*Journal of Zhejiang University-SCIENCE A 2026 27(4):400-416*
www.jzus.zju.edu.cn; www.springer.com/journal/11582
E-mail: jzus_a@zju.edu.cn

**Research Article**
https://doi.org/10.1631/jzus.A2500175

Check for updates

# Decomposition method for existing tunnel lining displacement induced by undercrossing: a case study

Yiming FU[1,2], Wenqi DING[1,2], Zhijian ZHAO[3], Wei LONG[3], Yafei QIAO[1,2]✉

[1]*Department of Geotechnical Engineering, College of Civil Engineering, Tongji University, Shanghai 200092, China*
[2]*Key Laboratory of Geotechnical and Underground Engineering of Ministry of Education, Tongji University, Shanghai 200092, China*
[3]*China Railway South Investment Group Co., Ltd., Shenzhen 518000, China*

**Abstract:** A decomposition method is proposed to divide the field monitoring displacement of tunnel linings into different components induced by dislocation, rotation, and elliptical deformation of the lining rings. Based on this method, a corresponding tunnel lining monitoring plan is also suggested. The key principles of the decomposition are the continuity of longitudinal deformation, the sinusoidal functional relationship between the rotation angle and the longitudinal distance to the cross point, and neglecting the longitudinal joint deformation. The proposed decomposition method was successfully applied to a metro project in China, and the decomposed pattern laws were discussed. The decomposed data indicate that the displacement of the lining ring is primarily influenced by elliptical deformation and dislocation, with elliptical deformation having the strongest impact. Moreover, the *z*-direction displacement of the existing tunnels linearly increases with the crossing angle, whereas the affected zone decreases nonlinearly. As for the lining ring rotation angle, its maximum value occurs during a 90° undercrossing scenario, and the rotation angles decrease nonlinearly as the crossing angle diminishes. Furthermore, the rotation angle first increases and then decreases as the distance from the crossing center increases. Temporally, the rotation angles follow a pattern of initial increase followed by gradual reduction. Regarding the ellipticity, the ellipticity increases with the crossing angle but decreases with distance from the crossing center. The findings of this study contribute to improved knowledge of tunnel lining displacement composition and monitoring. Future integration of our computational approach with total station monitoring systems could enable real-time monitoring, calculation, and analysis in tunnel engineering applications.

**Key words:** Displacement decomposition method; Shield tunnel; Field monitoring; Undercrossing; Crossing angle

## 1 Introduction

Newly constructed tunnels are increasingly crossing under existing metro lines in the development of urban metro systems. An improved understanding of tunneling-induced displacement of existing tunnels plays a crucial role in construction control, lining design, and reinforcement measures. Therefore, there has been significant research into the patterns of displacement induced by tunneling, which can be categorized into three groups according to their methodology: analytical solutions, numerical solutions, and field monitoring.

To understand tunneling-induced disturbances, numerous scholars have proposed theories of displacement for existing tunnels (Wanchai and Cho, 2005; Shen et al., 2014; Kumar et al., 2024; Yan et al., 2024). Some of these displacement theories described the relationship between settlement, rigid body displacement, and overall deformation (Zhang et al., 2016; Soomro et al., 2022). They explored the correlation between the settlement time-history development and construction activities, revealing the mechanisms of stress redistribution by quantifying deformation patterns and surface subsidence (Fang et al., 2015; Wei et al., 2018; Liu et al., 2021; Li et al., 2025). However, existing tunnel displacement theories have thus far only analyzed the developmental trends of displacement in existing tunnels. And these theories also have certain accuracy limitations, as some necessary and unavoidable assumptions.

To better replicate tunnel construction disturbances, refined finite element simulations have been conducted. These studies analyzed tunnel deformation

✉ Yafei QIAO, yafei.qiao@tongji.edu.cn
Yafei QIAO, https://orcid.org/0000-0001-7567-3988

Received May 8, 2025; Revision accepted Dec. 8, 2025;
Crosschecked Feb. 2, 2026; Online first Apr. 10, 2026

characteristics, surrounding soil pressure variations, and surface settlement behavior (Li et al., 2012; Dias and Kastner, 2013; Chen et al., 2018; Yin et al., 2018; Gao et al., 2024). Others investigated various influencing factors, such as the effects of crossing angles and vertical distances ($z$-distance) on the lining stress distribution, vault displacement patterns, surface settlement, and lining ring rotation (Galli et al., 2004; Li et al., 2016; Lai et al., 2020; Fang et al., 2024; Liu et al., 2024; Baishya and Choudhury, 2025). Finite element simulation results can be correlated with analytical solutions to enable more thorough analysis of the influence of earth pressure on segment deformation, thereby enhancing understanding of the composition of monitored displacements. However, precise finite element simulations require extensive foundational data analysis and prolonged model refinement to achieve accurate results. Moreover, finite element simulations cannot clearly describe issues such as the randomness of strata.

Therefore, analyzing monitoring data stands out as an intuitive method for judgment, providing foundational support for theoretical analysis and finite element simulations (Zhang et al., 2023; Cai et al., 2025). Deformation monitoring has been utilized to investigate construction methods, lining ring damage, deformation behaviors, and surface settlement, among other properties (Lee and Nam, 2001; Sharifzadeh et al., 2013; Fang et al., 2016; Huang et al., 2020). Compared to theoretical and numerical analyses, conclusions derived from deformation monitoring are more accurate and realistic, and thus offer reliable guidance for practical engineering applications (Lo and Ramsay, 1991; Li and Chen, 2012; Lin et al., 2013; Cao et al., 2018; Zhang et al., 2019; Zhang et al., 2020). However, deformation monitoring also exhibits a certain degree of dispersion, which complicates data analysis.

Under the disturbances from tunneling, an existing tunnel lining may settle, rotate, or deform, resulting in a complex displacement pattern. Although field monitoring data can provide more accurate values of displacement, methods to separate the displacement into different underlying patterns are still in development. Therefore, it is important to be able to effectively distinguish and quantify these components to accurately analyze the settlement of the lining ring and the opening of the segmental joint. Extensive research has investigated the displacement decomposition of lining rings. These include theoretical formulas incorporating rotation and dislocation mechanisms, and theoretical formulas prioritizing shear dislocation with secondary rigid rotation effects. Other studies introduced formulations that simultaneously consider segment rotation and oval deformation, complemented by stress evaluation methods unifying the influences of rotation and strain. For asymmetric loading scenarios, theoretical formulas have also been proposed to characterize the longitudinal bending-shear deformation of shield tunnel segments, improving the precision of displacement prediction in tunnel engineering (Wu et al., 2015; Wham et al., 2016; Wei et al., 2018; Liu et al., 2019; Wei et al., 2020; Huang and Zhou, 2023; Ding et al., 2024; Li et al., 2024; Zhang et al., 2024). Although some of the aforementioned studies investigated displacement decomposition, they did not fully consider displacement components. Displacement decomposition should integrate the three key factors of rotation, dislocation, and elliptical deformation. Not doing so hinders effective performance evaluation and maintenance strategy development for operational tunnels.

Therefore, in this study, we propose a displacement decomposition method for tunnel lining rings that incorporates dislocation, rotation, and elliptical deformation. This method is based on feedback analysis of monitoring data rather than forward theoretical derivations. Methods based on monitoring feedback analysis are more closely aligned with actual engineering conditions and better elucidate the components of lining ring displacement.

Using the proposed decomposition model, a comprehensive analysis is conducted on the ring displacements of the Shenzhen Metro Line 11 Phase II project, Shenzhen, China. Furthermore, the decomposed displacement data were examined to investigate the influence of the crossing angle and vertical clearance ($z$-distance) on the existing tunnel settlement, lining ring rotation, and elliptical deformation. This study enhances the understanding of lining ring displacement components, thereby aiding real-time monitoring and early warning systems and laying a theoretical foundation for the advancement of digital twin technology in tunnel engineering.

## 2 Displacement decomposition method

The monitored displacement of a tunnel lining is the combined result of the dislocation and rotation of

lining rings in the longitudinal direction and the elliptical deformation of lining rings in the cross-section. Determining the contribution of each factor to the measured displacement helps us understand the real deformation state of tunnels. Therefore, a new displacement decomposition method is proposed to back-analyze the dislocation, rotation, and elliptical deformation of lining rings.

### 2.1 Monitoring

Fig. 1 illustrates a suggested location for monitoring points on a tunnel lining. To accurately describe the elliptical deformation of lining rings, five coordinate points are a necessary minimum, which is what is used in this work. The coordinate system is defined as follows: the *x*-axis is oriented perpendicular to the lining ring plane and positive along the subway's operational direction; the *y*-axis represents the horizontal direction within the ring plane, and the positive direction is to the right; the *z*-axis corresponds to the vertical direction within the ring plane, and the upward direction is the positive direction. Monitoring point 1 (P1) and point 4 (P4) are positioned at the horizontal diameter extremities, point 5 (P5) is located at the crown position, and point 2 (P2) and point 3 (P3) are positioned at the railroad track alignment. Since tunnel operations and maintenance also require surveillance of rail displacement, using P2 and P3 can effectively reduce the workload associated with data monitoring. The intersection points between the concrete bed and the inner surface of the lining ring are defined as calculation point 6 (P6) and point 7 (P7). To minimize the impact of joints within the same lining ring on the displacement analysis, it is important to position at least two monitoring points on a single segment, such as P4 and P5.

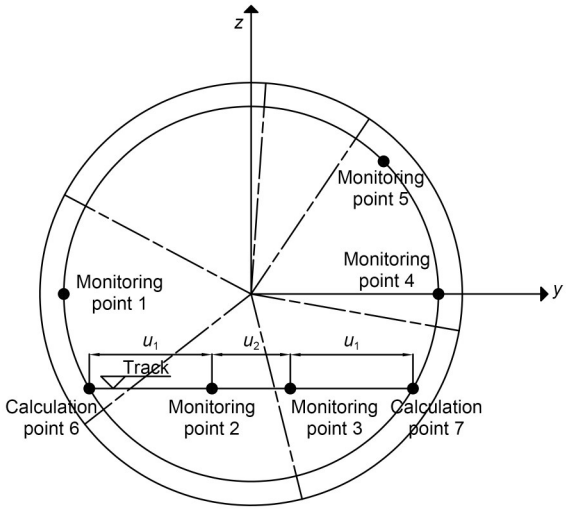


**Fig. 1 Schematic of the locations of the monitoring points on the *y*–*z* section**

The total station is usually set up in the tunnel, and the lining ring measurement point is approximately in the same straight-line direction. The angle between the line of sight and the tunnel axis is very small, causing the *x*-axis displacement in the measurement data to manifest as a small diagonal distance change, and making it difficult to distinguish from the ranging error. Thus, it is difficult for the total station to obtain reliable *x*-axis displacement measurements; the total station can only capture *y*- and *z*-axis displacements at each monitoring point. The symbols and coordinates of the five monitoring points are defined as P*n* ($y_n^k$, $z_n^k$), and the displacements of the monitoring points are $\Delta y_n^k$ and $\Delta z_n^k$. In this notation, *n* denotes the identification number of the monitoring point, while *k* represents the monitoring number. The formulas for the aforementioned symbols are given in Eqs. (1) and (2).

$$\Delta y_n^k = y_n^k - y_n^0, \quad n = 1,\ 2,\ 3,\ 4,\ 5, \tag{1}$$

$$\Delta z_n^k = z_n^k - z_n^0, \quad n = 1,\ 2,\ 3,\ 4,\ 5, \tag{2}$$

where ($y_n^0$, $z_n^0$) represent the initial coordinates of the monitoring point *n*. Based on the symmetric configuration of the monitoring system, the distance between P6 and P2 is maintained as equal to the distance between P7 and P3. Due to the high stiffness of the concrete foundation bed, it can be considered a rigid structure. Therefore, the displacements at P6 and P7 can be determined by applying Eqs. (3)–(6).

$$\Delta y_6^k = -\frac{(\Delta y_3^k - \Delta y_2^k)\,u_1}{u_2} + \Delta y_2^k, \tag{3}$$

$$\Delta z_6^k = -\frac{(\Delta z_3^k - \Delta z_2^k)\,u_1}{u_2} + \Delta z_2^k, \tag{4}$$

$$\Delta y_7^k = \frac{(\Delta y_3^k - \Delta y_2^k)\,u_1}{u_2} + \Delta y_3^k, \tag{5}$$

$$\Delta z_7^k = \frac{(\Delta z_3^k - \Delta z_2^k)\,u_1}{u_2} + \Delta z_3^k, \tag{6}$$

where $u_1$ represents the linear distance between P6 and P2 and $u_2$ denotes the distance between P2 and P3 (Fig. 1).

### 2.2 Displacement decomposition mode

Fig. 2 presents a schematic representation of the displacement decomposition methodology. The displacement characteristics of existing tunnel lining systems can be decomposed into three primary components: dislocation, rotation, and elliptical deformation.

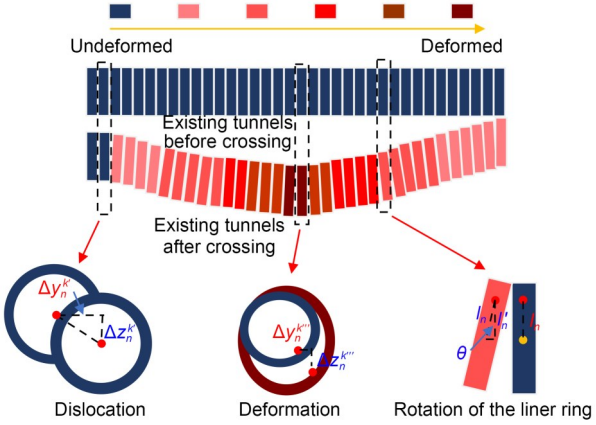


**Fig. 2 Displacement decomposition**

Regarding dislocation, all five monitoring points on the lining ring have identical horizontal ($\Delta y_n^{k'}$) and vertical ($\Delta z_n^{k'}$) displacement components, maintaining their relative positions throughout the movement. Considering rotational displacement, each monitoring point has a vertical displacement component ($\Delta z_n^{k''}$) that is directly proportional to its position relative to the center of rotation. The magnitude of this vertical displacement can be determined by Eq. (7).

$$\Delta z_n^{k''} = l_n - l_n \cos\theta, \tag{7}$$

where $\theta$ represents the rotation angle and $l_n$ represents the $z$-directional distance between the monitoring point $n$ and the center of the lining ring before deformation.

Structural deformation of the lining ring manifests as position-dependent displacement variations, characterized by distinct horizontal ($\Delta y_n^{k'''}$) and vertical ($\Delta z_n^{k'''}$) components at each monitoring point. Therefore, the horizontal and vertical displacements of the five monitoring points can be decomposed into the following components:

$$\Delta y_n^k = \Delta y_n^{k'} + \Delta y_n^{k'''}, \tag{8}$$

$$\Delta z_n^k = \Delta z_n^{k'} + \Delta z_n^{k''} + \Delta z_n^{k'''}. \tag{9}$$

### 2.3 Rotation of the lining ring

The difference in the $z$-directional distance between P4 and P5 is primarily influenced by the rotation of the lining ring and the elliptical deformation. The rotation of the lining ring can be determined by decomposing the change in the $z$-directional distance between P4 and P5 ($\Delta z_{45}^k$), which is calculated by Eq. (10).

$$\Delta z_{45}^k = \Delta z_5^k - \Delta z_4^k. \tag{10}$$

Considering the rotation and deformation of three consecutive lining rings as illustrated in Fig. 3—where the three lining rings are labeled a, b, and c—the rotation angle of the lining ring is denoted as $\theta_n$. Eq. (11) yields the $z$-directional distance between P4 and P5 before deformation ($l_{45}$):

$$l_{45} = l_5 - l_4. \tag{11}$$

Consequently, the difference in the $z$-directional distance between P4 and P5 can be expressed as follows:

$$\Delta z_{45}^k = (l_{45} + l_{45n\text{-d}}^k)\cos\theta_n - l_{45}, \tag{12}$$

where $l_{45n\text{-d}}^k$ represents the increment in $l_{45}$ resulting from the elliptical deformation of the lining ring.

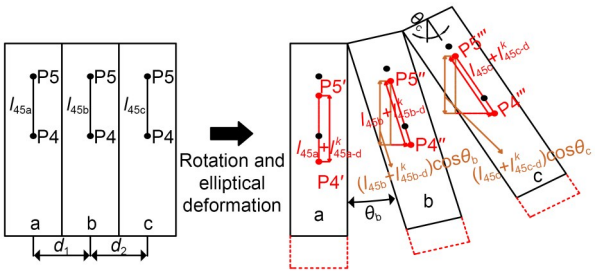


**Fig. 3 Combined displacement due to the rotation and deformation**

When an existing tunnel is subjected to a disturbance, the rotation angle at the center of the disturbance is 0°, and the rotation curve of the existing tunnel is continuous. The rotation angle of the lining rings as a function of the distance between the disturbance center and the far endpoint (where the rotation angle returns to 0°) can be approximated as a sinusoidal curve (Zhang, 2020; Zhang et al., 2022). Therefore, to facilitate the decomposition of the rotation and oval deformation of the lining rings, the following assumptions are made:

(1) The rotation angle of the lining ring at the crossing center of the existing tunnel is 0°, as seen for lining ring a in Fig. 3.

(2) The rotation angle of the lining ring is a sinusoidal function of the distance to the crossing center, and its derivative is a cosine function. As illustrated in Fig. 3, the rotation angles of lining rings a, b, and c follow sinusoidal functions for their distances to the crossing centers.

Considering the constraining effect between adjacent lining rings, the $l^k_{45n\text{-d}}$ of lining rings a, b, and c is a continuous function:

$$l^k_{45\text{b-d}}=\frac{d_1 l^k_{45\text{b-c}}+d_2 l^k_{45\text{b-a}}}{d_1+d_2}, \tag{13}$$

where $d_1$ is the distance between the centers of lining rings a and b, and $d_2$ is the distance between the centers of lining rings b and c.

Eq. (14) is used to calculate the distance between the disturbance center and the far endpoint, where the rotation angle returns to 0° (Zhang et al., 2022):

$$S=0.9h\tan\left(45°+\frac{\varphi}{2}\right), \tag{14}$$

where $S$ represents the distance from the disturbance center to the far endpoint where the rotation angle returns to 0°, $h$ is the difference in burial depth between the existing tunnel and the new tunnel, and $\varphi$ represents the internal friction angle of the soil layer. The secant slope between two points on the curve is approximately equal to the tangent slope at the midpoint of the two points, as expressed by the following:

$$\frac{\left.\frac{\partial\theta}{\partial d}\right|_{d=\frac{d_1}{2}}}{\left.\frac{\partial\theta}{\partial d}\right|_{d=\frac{d_2}{2}+d_1}}=\frac{\frac{\theta_\text{b}}{d_1}}{\frac{\theta_\text{c}-\theta_\text{b}}{d_2}}=\frac{\cos\left(\frac{d_1}{2S}\pi\right)}{\cos\left(\frac{\frac{d_2}{2}+d_1}{S}\pi\right)}. \tag{15}$$

By substituting the rotation angles and deformations of lining rings b and c into Eq. (15), Eqs. (16) and (17) can be derived:

$$\Delta z^k_{45\text{b}}=(l_{45\text{b}}+l^k_{45\text{b-d}})\cos\theta_\text{b}-l_{45}, \tag{16}$$

$$\Delta z^k_{45\text{c}}=(l_{45\text{c}}+l^k_{45\text{c-d}})\cos\theta_\text{c}-l_{45}. \tag{17}$$

By solving the system of equations (Eqs. (13)–(17)) using MATLAB, the rotation angle of lining ring b can be determined. Subsequently, through application of the same computational method to solve the systems of equations for the following two rings, the rotation angle of lining ring c can be obtained. By repeating this calculation process along the tunnel, the rotation angles of all the lining rings can be determined sequentially. Once the rotation angles of the lining rings are determined, $\Delta z^{k''}_n$ can be derived using Eq. (7).

### 2.4 Dislocation of the lining ring

The track is supported by a concrete bed beneath the rails. Under the condition that no cracks develop between the concrete bed and the lining ring, the concrete bed can be considered as a rigid body structure; consequently, the concrete bed is resistant to deformation. The monitoring data at P2 and P3 are similar, and thus, one can assume that the two monitoring points on the concrete bed only undergo dislocation and rotation of the lining ring. The rotation of the lining ring does not affect the $y$-direction dislocation, instead only influencing the $z$-direction dislocation. Therefore, the dislocation magnitude of the lining ring can be obtained by eliminating the rotational effects from the average displacement changes at P2 and P3. The values calculated from Eqs. (18) and (19) represent the internal structural dislocation of the lining ring.

$$\Delta y^{k'}_n=\frac{\Delta y^k_2+\Delta y^k_3}{2}, \tag{18}$$

$$\Delta z^{k'}_n=\frac{\Delta z^k_2+\Delta z^k_3}{2}-l_2\sin(\theta^k_n)\tan\left(\frac{\theta^k_n}{2}\right), \tag{19}$$

where $\theta^k_n$ represents the rotation angle generated by lining ring $n$ at time $k$.

### 2.5 Elliptical deformation of the lining ring

Using Eqs. (8) and (9), $\Delta z^{k'''}_n$ and $\Delta y^{k'''}_n$ can be computed accordingly. Based on this result, the post-deformation elliptical configuration of the lining ring (including the geometric parameters of its major and minor axes) can be precisely determined through fitting analysis. This analysis, performed in MATLAB, utilizes the spatial coordinates of P1, P4, P5, P6, and P7, where the coordinates of P6 and P7 are derived from the coordinates of P2 and P3 using Eqs. (20)–(23). The degree of elliptical deformation of the lining ring is then calculated using Eq. (24).

$$y_6=-\frac{(y_3-y_2)u_1}{u_2}+y_2, \tag{20}$$

$$z_6=-\frac{(z_3-z_2)u_1}{u_2}+z_2, \tag{21}$$

$$y_7=\frac{(y_3-y_2)u_1}{u_2}+y_3, \tag{22}$$

$$z_7=\frac{(z_3-z_2)u_1}{u_2}+z_3, \tag{23}$$

$$e=\frac{r_1-r_2}{2R}, \tag{24}$$

where $e$ is the ellipticity, $r_1$ is the length of the long axis, $r_2$ is the length of the short axis, and $R$ is the radius of the lining ring.

### 2.6 Summary and discussion

The proposed calculation method holds true under the following assumptions:

(1) The rotation angle of the lining ring at the crossing center of the existing tunnel is 0°.

(2) The rotation angle of the lining ring is a sinusoidal function of the distance to the crossing center, and its derivative is a cosine function.

(3) The deformation caused by longitudinal joints in the lining rings can be neglected.

(4) Considering the constraining effect between adjacent lining rings, the $l^k_{45n\text{-d}}$ of adjacent lining rings is a continuous function.

Fig. 4 presents a calculation flowchart of the above displacement decomposition method. The steps of the method are as follows: First, from the displacement monitoring data at P4 and P5, the rotation angle of the lining ring is calculated based on the deformation-rotation compatibility equations, $z$-direction displacement difference decomposition equations, and the mentioned assumptions. However, it should be noted that engineering uncertainties and stochastic factors can lead to errors in calculating the rotation angles. Then, after calculating the average value of the displacement monitoring data at P2 and P3, the dislocation of adjacent lining rings is determined by removing the influence of the lining ring rotation. Finally, the rotation angles and dislocation of the lining ring are substituted into Eqs. (8) and (9) to calculate the deformation components of the displacements of the five nodes on the lining ring. Then, the ellipticity of the lining ring is obtained through curve fitting in MATLAB.

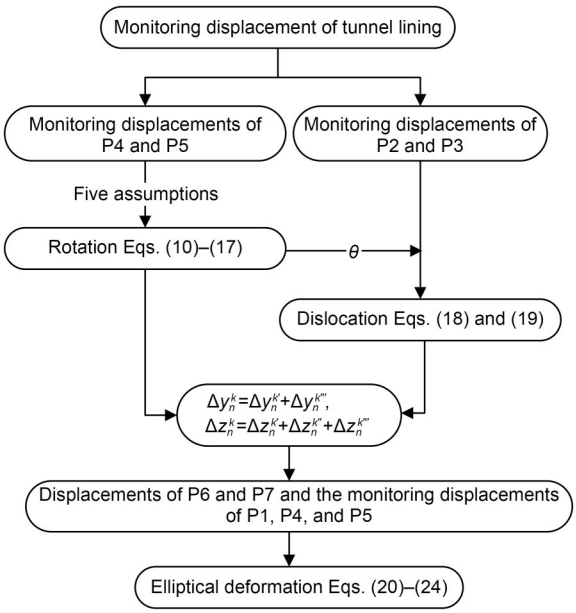


**Fig. 4 Flowchart describing the displacement decomposition method**

## 3 Project overview

### 3.1 Route of the tunnel

The Shenzhen Metro Line 11 Phase II Project, which lies between the Eighth Affiliated Hospital of Sun Yat-sen University Station (project name) and Gangxia North Station, Shenzhen, China, comprises a left tunnel with a total length of about 1054 m and a right tunnel extending about 1105 m. Fig. 5 illustrates the route of the project and the monitoring areas for the existing tunnels. The right tunnel of Line 11 first perpendicularly crosses the left and right tunnels of Line 1, which is followed by a crossing at an angle of 14° with the exit tunnel of Line 14, and finally, a parallel crossing with the Line 14 exit tunnel. For the left tunnel of Line 11, the sequence begins with a crossing of the Line 14 exit tunnel at an angle of 59°, followed by a crossing of the Line 14 admission tunnel at 24°, and finally with a perpendicular crossing of the left and right tunnels of Line 1. Since there are many tunnels in this section, diverse crossing angles, complex geological conditions, and Line 1 has been in operation for a long time, the application, in the Shenzhen Metro Line 11 Phase II Project, of the proposed displacement decomposition model holds significant research value.

Shenzhen Metro Line 1 was constructed in 2004 using the cut-and-cover method, while Shenzhen Metro

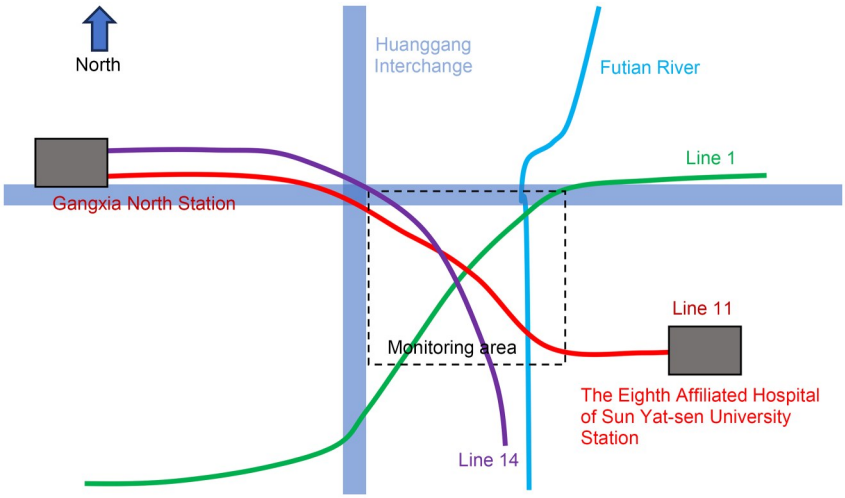


**Fig. 5 Locations and monitoring zones of existing and new tunnels**

Line 14 was constructed in 2022 using the shield tunneling method. These lines differ in two key aspects: (1) Construction method. The cut-and-cover method used for Line 1 typically results in a structure with lower overall stiffness and integrity compared to the modern shield-tunneled segments of Line 14. This makes Line 1 more sensitive structurally to disturbances from below. (2) Ground conditions and burial depth. Line 1 has a shallower burial depth than Line 14. The influence of the new tunnel (Line 11) on the deeper Line 14 is relatively larger than that in Line 1. In terms of the impact on shallower Line 1, the presence of the deeper Line 14 itself acts as a mitigating factor, effectively reducing the disturbance transferred from the new construction to Line 1 above.

### 3.2 Construction program

The Line 11 tunnel employs an earth pressure balance (EPB) shield machine, characterized by an excavation diameter of 6.48 m. The tunnel is situated at varying overburden depths ranging from 10.8 to 13.5 m. The shield tunnel lining segment has an inner diameter of 5.5 m, an outer diameter of 6.2 m, and a width of 1.5 m, and the tunnel lining ring is composed of six segments. The segments are installed using a staggered joint configuration to enhance the structural integrity. The EPB shield machine operates under controlled parameters: the soil chamber pressure is maintained at approximately 290 kPa to ensure stability of the face, while the grouting pressure is regulated at around 320 kPa to optimize ground consolidation and minimize disturbance. The cutter head torque is controlled at approximately 2000 kPa to maintain efficient excavation performance while preventing excessive ground disturbance. The chamber pressure, grouting pressure, and cutterhead torque are dynamically adjusted in response to changes in the shield machine's tunneling depth.

### 3.3 Geological conditions

Fig. 6 presents a stratigraphic cross-section illustrating the geological structure and geotechnical parameters along vertical profiles; more details on the geotechnical parameters are listed in Table 1. The geological profile above the shield tunnel—in descending stratigraphic order—is comprised of the following distinct layers: stockpile soil, silty sand, grit, gravelly clayey soil, fully weathered granite, strongly weathered granite, moderately weathered granite, and weakly weathered granite. Line 14 primarily traverses through silty sand and grit, and Line 1 is mainly situated in fully weathered granite. Line 11 predominantly passes through weakly weathered granite, intermittently encountering less competent strata such as gravelly clay, coarse sand, and medium sand layers.

### 3.4 Monitoring program

To better apply the proposed displacement decomposition method, the following monitoring point arrangement was implemented on Line 1 and Line 14 of the Shenzhen Metro. The monitoring points of Line 1 and Line 14 are illustrated in Fig. 7 ($\beta$ is the crossing angle). The spacing between monitoring sections ranges from 4.5 to 10.0 m, with an appropriate

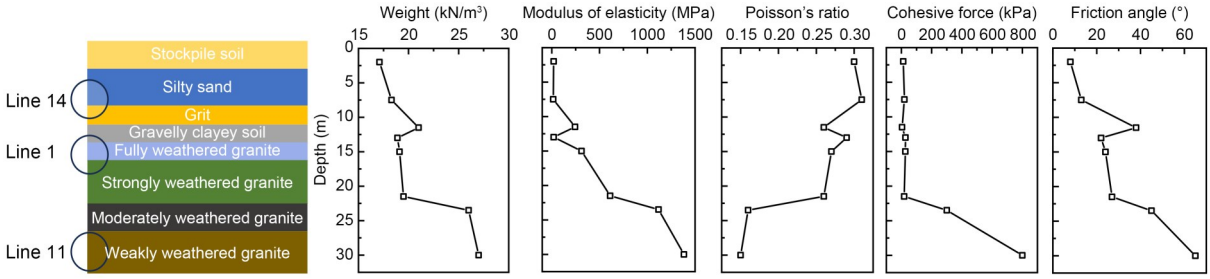


**Fig. 6 Soil profile and geotechnical parameters along the depth direction**

**Table 1 Geotechnical parameters**

| Soil layer name | Thickness (m) | Modulus of elasticity (MPa) | Poisson's ratio | Cohesive force (kPa) | Friction angle (°) | Weight (kN/m$^3$) |
|---|---|---|---|---|---|---|
| Stockpile soil | 2.0 | 20 | 0.30 | 12 | 8 | 17.1 |
| Silty sand | 5.5 | 15 | 0.31 | 20 | 13 | 18.3 |
| Grit | 4.0 | 244 | 0.26 | 4 | 38 | 21.0 |
| Gravelly clayey soil | 1.5 | 20 | 0.29 | 27 | 22 | 18.9 |
| Fully weathered granite | 2.0 | 312 | 0.27 | 26 | 24 | 19.1 |
| Strongly weathered granite | 6.5 | 611 | 0.26 | 18 | 27 | 19.5 |
| Moderately weathered granite | 2.0 | 1118 | 0.16 | 300 | 45 | 26.0 |
| Weakly weathered granite | – | 1384 | 0.15 | 800 | 65 | 27.0 |

densification of monitoring points established in the crossing area. There are 18 total monitoring sections distributed along both the left and right tunnels of Line 1, complemented by 20 monitoring sections on Line 14's entrance tunnel and 37 monitoring sections on its exit tunnel. Using the displacement decomposition method proposed in this study, each monitoring section was instrumented with five monitoring points, as illustrated in Fig. 7a.

The designated monitoring area was located at the intersection zone where Metro Line 11 crosses both Lines 1 and 14. Table 2 summarizes the key parameters of the five monitoring areas within the crossing zone, including the crossing angle, vertical ($z$-direction) tunnel separation distance, monitoring duration, cross-section number at the crossing center, and crossing time. The monitoring areas include:

(1) Monitoring area 1: the area where the right tunnel of Line 11 runs the exit tunnel of Line 14 in parallel, as illustrated in Fig. 7c.

(2) Monitoring area 2: the area where the right tunnel of Line 11 crosses the exit tunnel of Line 14 at an angle of 14°, and S23 is the crossing section, as illustrated in Fig. 7d.

(3) Monitoring area 3: the area where the left tunnel of Line 11 crosses the admission tunnel of Line 14 at an angle of 24°, and $S6_{ad}$ is the crossing section, as illustrated in Fig. 7e.

(4) Monitoring area 4: the area where the left tunnel of Line 11 crosses the exit tunnel of Line 14 at an angle of 59°, and $S6_{ex}$ is the crossing section, as illustrated in Fig. 7f.

(5) Monitoring area 5: the area where the right tunnel of Line 11 perpendicularly crosses the left tunnel of Line 1, and S14 is the crossing section, as illustrated in Fig. 7g.

## 4 Monitoring data and displacement decomposition results

To prevent the main body of the results section from becoming excessively lengthy, the detailed calculation procedures for the monitoring data are shown in Tables S1–S4 of the electronic supplementary materials (ESM).

### 4.1 Settlement of the lining ring

The settlements of the existing tunnel at the five monitoring sections are presented in Fig. 8. It is important to note that the settlement herein does not mean the dislocation between individual lining rings,

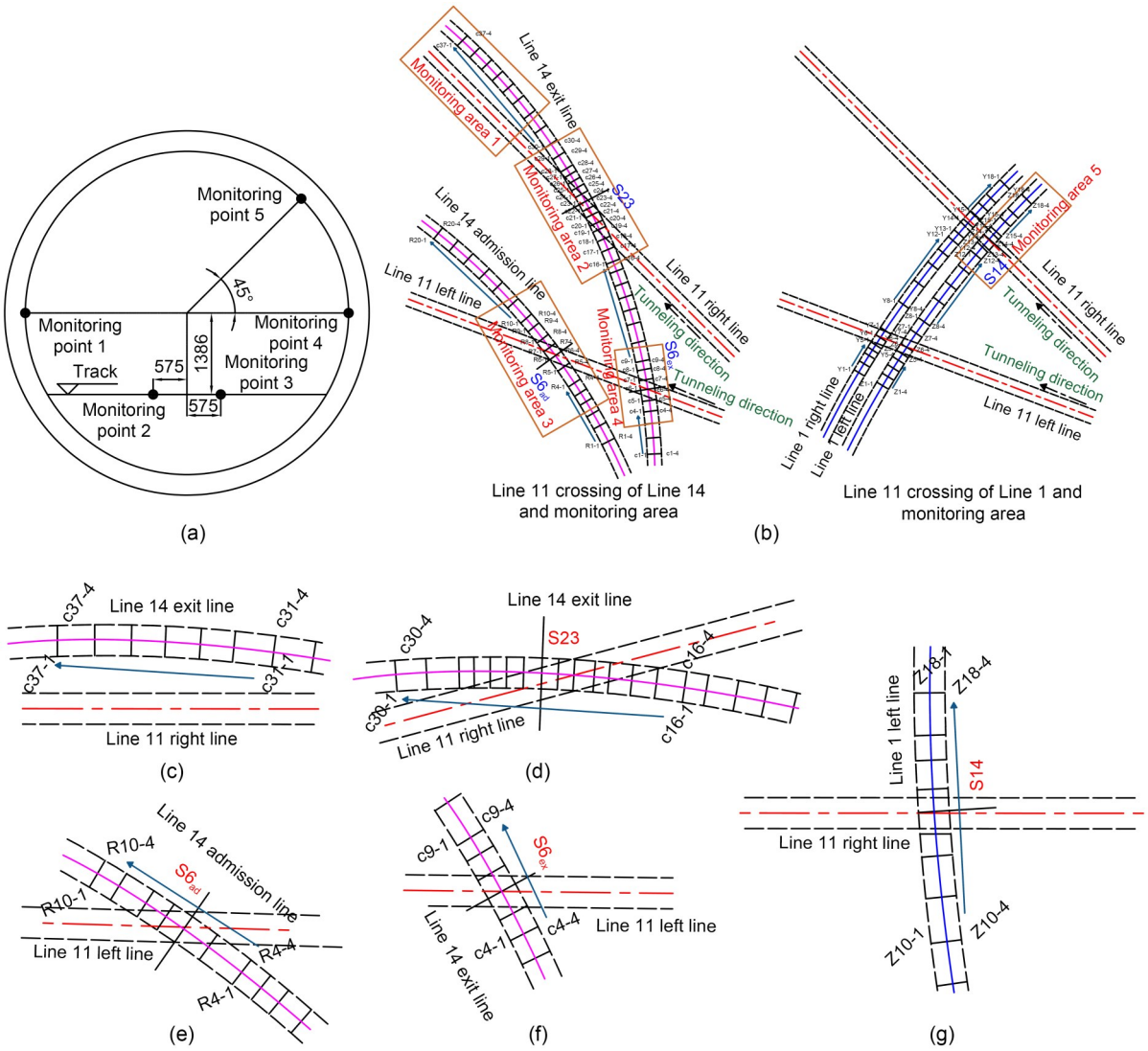


**Fig. 7 Monitoring points and monitoring areas: (a) layout of monitoring points in the lining ring (unit: mm); (b) monitoring areas of Line 1, Line 11, and Line 14 (m); (c) monitoring area 1 ($\beta$=0°); (d) monitoring area 2 ($\beta$=14°); (e) monitoring area 3 ($\beta$=24°); (f) monitoring area 4 ($\beta$=59°); (g) monitoring area 5 ($\beta$=90°)**

**Table 2 Key parameters of the five monitoring areas**

| Monitoring area | Crossing angle, $\beta$ (°) | $z$-direction distance (m) | Monitoring duration (year: 2023) | Cross-section number at the crossing center | The moment of passing through the center |
|---|---|---|---|---|---|
| 1 | 0 | 25.0 | June 7 to June 16 | – | – |
| 2 | 14 | 25.0 | May 20 to May 30 | S23 | May 26 |
| 3 | 24 | 25.0 | April 19 to May 1 | $S6_{ad}$ | April 27 |
| 4 | 59 | 25.0 | April 12 to April 25 | $S6_{ex}$ | April 22 |
| 5 | 90 | 17.2 | May 20 to June 2 | S14 | May 26 |

as in Section 2.4. The settlement of the lining ring concrete bed is affected by both the rotation angle of the lining ring and the dislocation of the lining ring. As the monitoring sections are not uniformly distributed across every lining ring, only the settlement of the lining ring can be analyzed. Therefore, for the present problem, the settlement ($\Delta s_n^k$) calculations follow:

$$\Delta s_n^k = \frac{\Delta z_2^k + \Delta z_3^k}{2}. \tag{25}$$

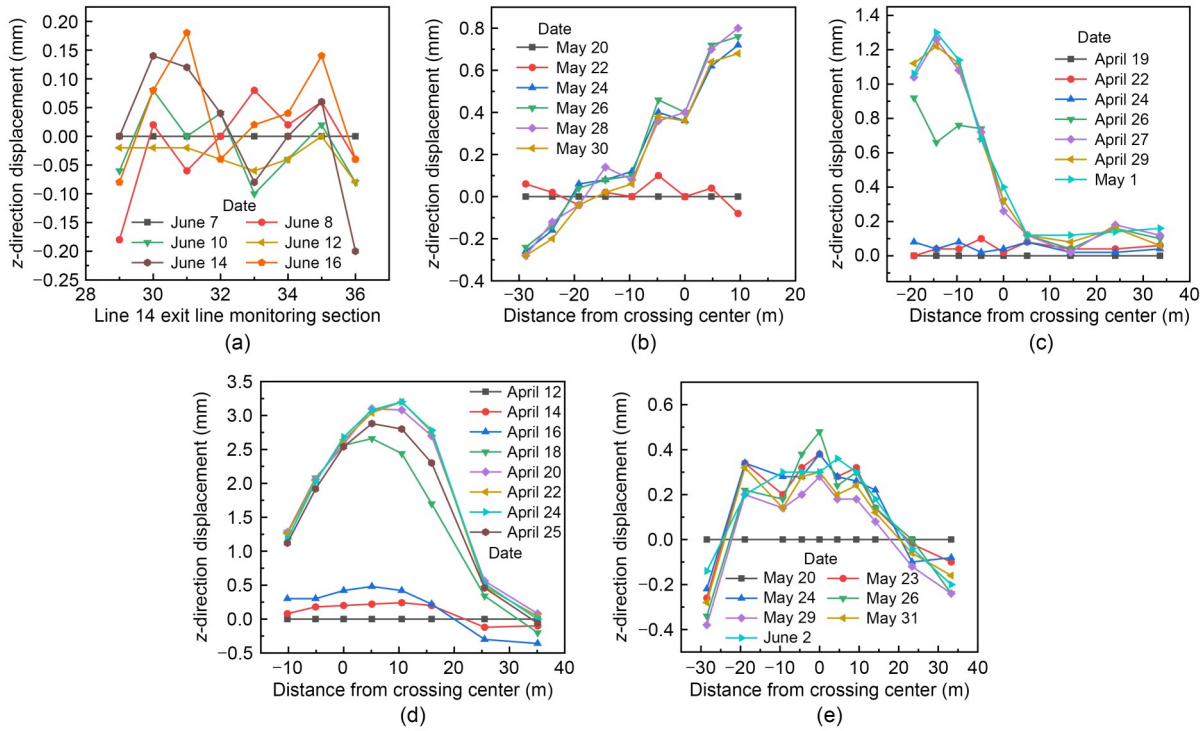


**Fig. 8 $z$-direction displacements of the lining ring: (a) monitoring area 1 ($\beta$=0°); (b) monitoring area 2 ($\beta$=14°); (c) monitoring area 3 ($\beta$=24°); (d) monitoring area 4 ($\beta$=59°); (e) monitoring area 5 ($\beta$=90°)**

In this section, downward displacement (toward the new tunnel) is defined as positive. The influence range of the new tunnel was determined to be the distance between the point where the settlement becomes zero and the front and the back of the crossing center. When the shield machine is located more than 50 m away from the crossing center, its influence on the central section becomes negligible. With the shield advancing at a rate of approximately 5 m/d, the $z$-direction settlement of the lining ring was analytically reset to zero about 10 d before the machine arrived at the central cross-section for convenience (Zhang et al., 2022).

Fig. 8 shows the time-history curves of the $z$-direction settlement of the existing tunnel for undercrossing at different angles. The maximum $z$-direction settlement is: 0.15 mm for parallel crossing, 0.80 mm at 14°, 1.30 mm at 24°, and 3.00 mm at 59°. The relationship between the $z$-direction settlement, influence range, and crossing angle is presented in Fig. 9. The results demonstrate that the maximum settlement increases linearly with crossing angle, while the influence range decreases in a nonlinear fashion as the crossing angle increases.

Fig. 8a demonstrates that the settlements along different sections of Line 14 exhibit uniform temporal

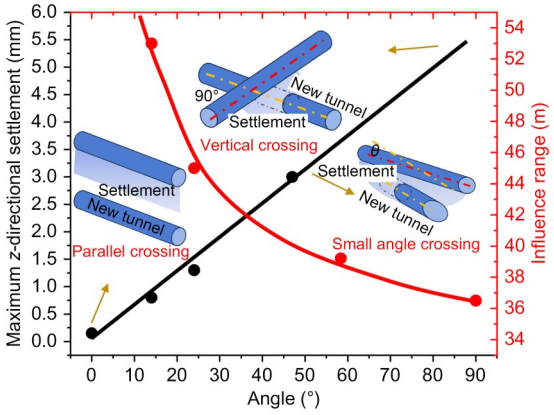


**Fig. 9 Relationship between the $z$-direction settlement, influence range, and crossing angle**

variations. Consequently, the disturbances induced by the parallel undercrossing in the existing tunnel display no discernible spatiotemporal patterns, instead manifesting as random fluctuations. In contrast, the small-angle undercrossings produce significantly disturbed patterns in the existing tunnel structure. Thus, parallel undercrossing is more relevant to the continuity of the $z$-direction settlement of the existing tunnel, while perpendicular undercrossing is more relevant to new tunnel crossings.

When the crossing angle was 59°, prior to crossing, the *z*-direction settlement in the section was nearly zero. During crossing, the *z*-settlement rapidly increased to 3.00 mm, which was followed by a slight decrease to 2.75 mm after the crossing was complete, as illustrated in Fig. 8d. This 8.3% rebound demonstrates the partial recovery effect of grouting and other stabilization measures on existing tunnel deformation. As the crossing angle reaches 90°, −0.40 mm of settlement occurs at locations that are 30 m away, indicating that vertical undercrossing induces upward deformation (reverse buckling) of the existing tunnel at these distant positions, as illustrated in Fig. 8e.

### 4.2 Rotation of the lining ring

Theoretically, a parallel undercrossing does not induce lining ring rotation in existing tunnels. Therefore, our rotational analysis focuses exclusively on monitoring areas 2–5. Fig. 10 illustrates the rotation angles of the lining rings, calculated by Eqs. (10)–(17), in monitoring areas 2–5 at different monitoring times; here, positive values indicate leftward rotation from the crossing center, and negative values denote rightward rotation toward the crossing center. When the crossing angle is 14°, the maximum rotation angle of the lining ring reaches $0.75\times10^{-3}$ (°). This increases to $1.07\times10^{-3}$ (°) at 24°, $1.01\times10^{-3}$ (°) at 59°, and peaks at $1.11\times10^{-3}$ (°) for the 90° crossing. Fig. 11 depicts this nonlinear relationship between crossing angle and maximum lining ring rotation angle.

Analysis of the 24° undercrossing case (Fig. 10b) reveals the spatiotemporal evolution of the lining ring rotation angle. The lining ring rotation angle initially increases and then decreases with increasing distance from the undercrossing center. The rotation angle exhibits a rapid initial increase followed by a gradual decrease.

### 4.3 Elliptical deformation of lining rings

To investigate the variation in ellipticity in a single lining ring under different crossing angles over time, this section presents the ellipticity versus time curves

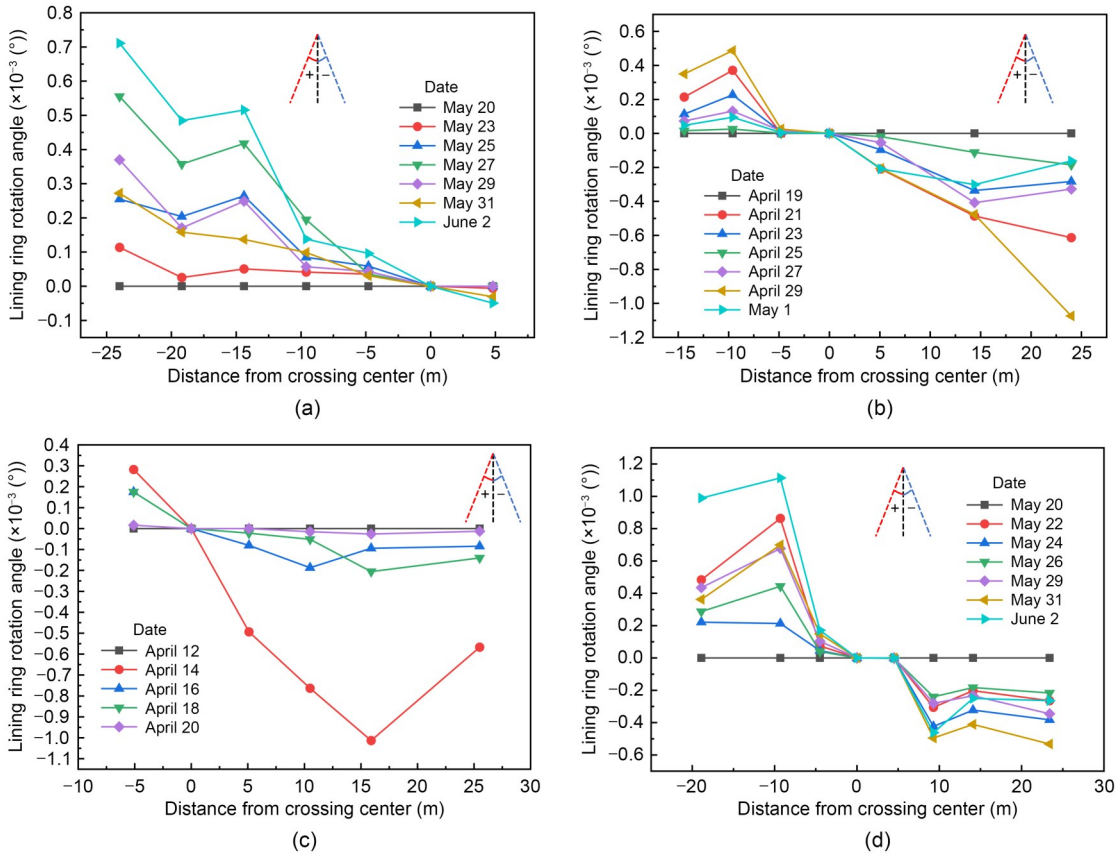


**Fig. 10 Rotation angles of the lining rings in monitoring areas 2–5: (a) monitoring area 2 ($\beta$=14°); (b) monitoring area 3 ($\beta$=24°); (c) monitoring area 4 ($\beta$=59°); (d) monitoring area 5 ($\beta$=90°)**

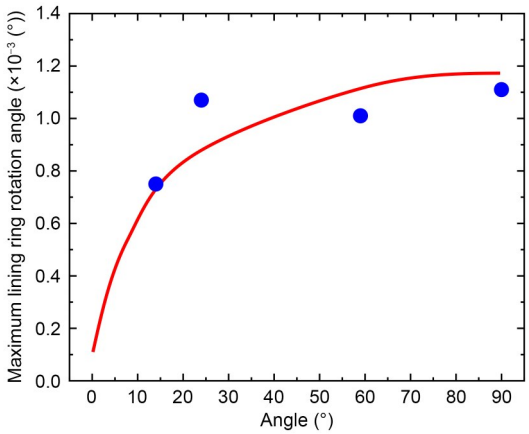


**Fig. 11 Relationship between the crossing angle and the maximum lining ring rotation angle**

for S23 in monitoring area 2, $S6_{ad}$ in monitoring area 3, $S6_{ex}$ in monitoring area 4, and S14 in monitoring area 5, as shown in Fig. 12. These curves demonstrate two distinct patterns, which are determined by the magnitude of the crossing angle. For a small crossing angle, the ellipticity initially increases rapidly before stabilizing. During the stabilization phase, significant fluctuations in ellipticity are observed (Figs. 12a and 12b). In contrast, for a large crossing angle, the ellipticity first rises sharply and then gradually stabilizes. During the stabilization phase, fluctuations in the ellipticity are relatively minor (Figs. 12c and 12d). When the crossing angle is small, the influence of the newly constructed tunnel persists for an extended period. In contrast, a large crossing angle leads to a shorter-lived impact. Therefore, the duration of influence emerges as the predominant factor governing the magnitude of the ellipticity fluctuations.

Based on the time-dependent ellipticity curves of multiple lining rings, Fig. 13 illustrates the spatial distribution of ellipticity and its evolution over time. The maximum measured ellipticity values are 1.7‰, 3.0‰, and 6.5‰ at crossing angles of 14°, 24°, and

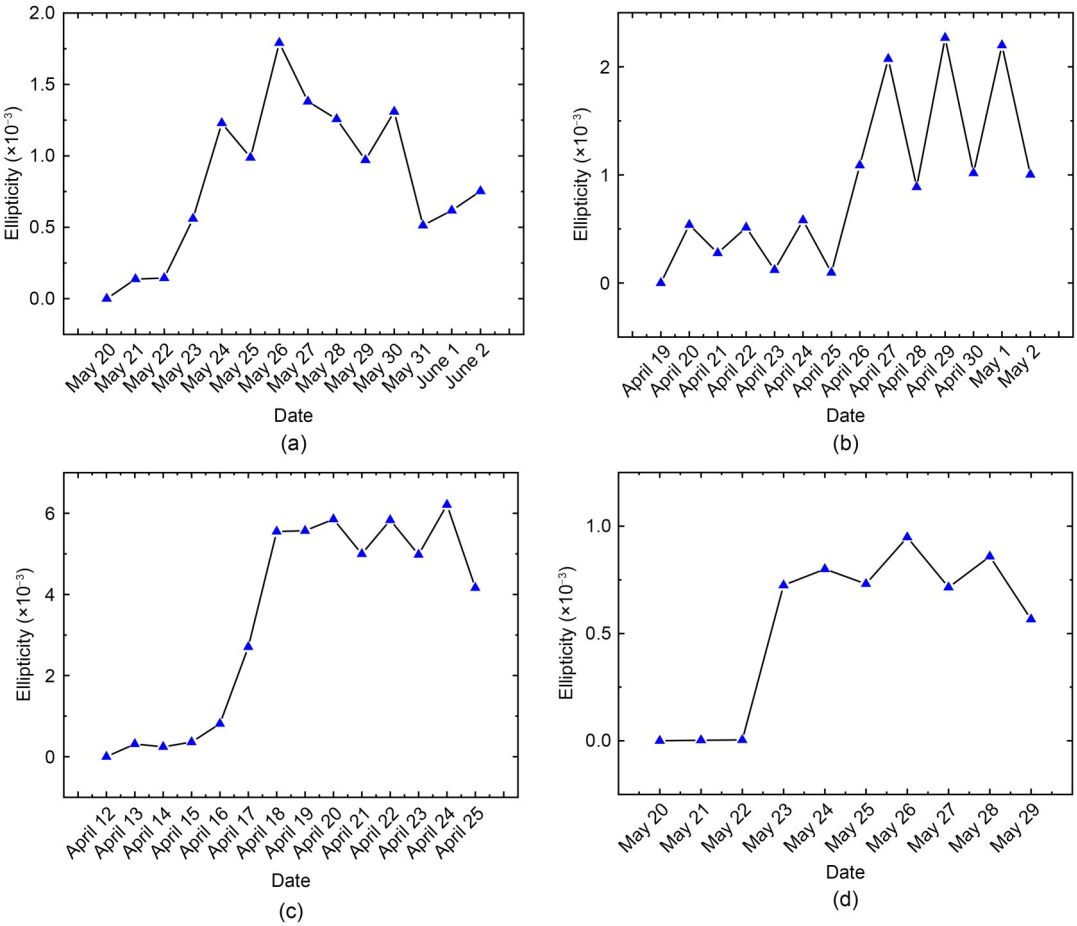


**Fig. 12 Ellipticity versus time curves of the crossing sections in four monitoring areas: (a) monitoring area 2 ($\beta$=14°); (b) monitoring area 3 ($\beta$=24°); (c) monitoring area 4 ($\beta$=59°); (d) monitoring area 5 ($\beta$=90°)**

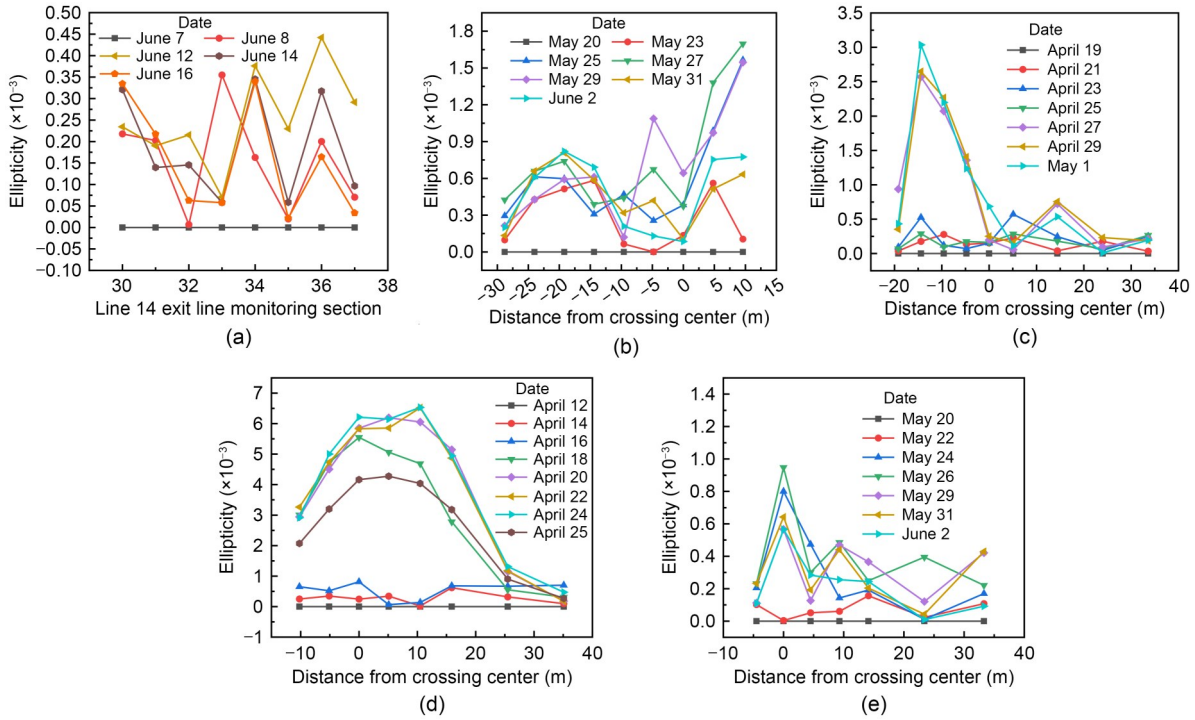


**Fig. 13 Variation curve of ellipticity for each section: (a) monitoring area 1 ($\beta$=0°); (b) monitoring area 2 ($\beta$=14°); (c) monitoring area 3 ($\beta$=24°); (d) monitoring area 4 ($\beta$=59°); (e) monitoring area 5 ($\beta$=90°)**

59°, respectively. These results demonstrate that the maximum ellipticity increases with crossing angle. However, as depicted in Fig. 13e, when the crossing angle is 90°, the maximum ellipticity is 1.0‰, which is lower than the values under smaller crossing angles. When the crossing angle is 90°, the existing tunnel analyzed under the small-angle crossing is Line 1, not Line 14. However, based on the engineering context, significant differences exist between Line 14 and Line 1 in terms of construction methods, ground conditions, and the distance between the existing and newly constructed tunnels. Therefore, the maximum ellipticity depends not only on the crossing angle but also on such variables.

When the crossing angles are 59° and 90°, as illustrated in Figs. 13d and 13e, respectively, the ellipticity of the lining rings decreases with increasing distance to the crossing center. However, this spatial distribution does not hold for the 14° and 24° undercrossing cases. While generally the ellipticity variation decreases with increasing distance, the unusual pattern identified in this case was primarily caused by grouting activities compensating for ground loss, resulting in fluctuations in the lining ring deformation. In addition, construction randomness and other uncertainties likely influenced this behavior. Thus, the ellipticity variation in the lining rings is influenced not only by tunnel excavation but also by factors such as grouting conditions and shield machine attitude adjustments.

Subsequently, based on the elliptical deformation fitting results of the lining rings, the relationship between the relative position of the new tunnel and the existing tunnel, as well as the direction of the elliptical major axis, can be analyzed. In this section, a case in which the right line of Line 11 perpendicularly crosses the left line of Line 1 is selected for analysis. As illustrated in Fig. 14, when Line 11 is excavated up to cross-section a, the major axis of the elliptical deformation in the calculated left-line section of Line 1 points toward cross-section a of Line 11. Next, as Line 11 advances to cross-section b, the major axis of

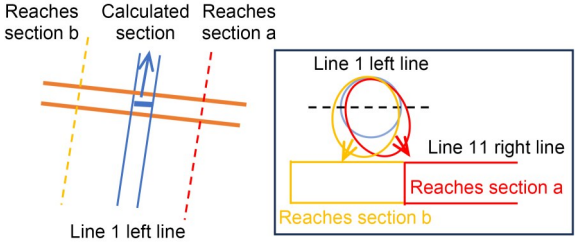


**Fig. 14 Long axis of the tunnel section ellipse points**

the elliptical deformation in the left-line section of Line 1 deviates from its original orientation, shifting toward cross-section b of Line 11. This indicates that the long axis of the ellipse of the existing tunnel section is often oriented toward the excavation face of the new tunnel.

### 4.4 Discussion

The proposed displacement decomposition method can be effectively applied to tunnel crossings at various angles, enabling rapid decomposition of lining ring displacements into three components: dislocations, rotations, and deformations. Leveraging this method enables more accurate assessments of the tunnel's bearing state, thereby facilitating the selection of appropriate emergency countermeasures for different risk scenarios. Future integration of this computational approach with total stations could enable real-time monitoring, calculation, and analysis. Nevertheless, there are several limitations caused by engineering uncertainties, random factors, and excessive deformation that should be acknowledged. The inverse analysis of known lining ring rotations and displacements demonstrates that the rotation angle follows a sinusoidal function with respect to distance. However, engineering uncertainties and stochastic factors inevitably introduce errors into the rotation angle calculations. For one, the lining rings are assumed to be homogeneous circular rings in our analysis. But when excessive deformation occurs, this assumption may not hold true, and errors may be introduced into the ellipticity calculations. For areas with significant deformation, targeted high-precision monitoring measures should be implemented. Our analysis also assumes that there is no deformation in the tracks and the concrete bed. However, this assumption becomes invalid when excessive lining ring deformation occurs, particularly if cracks develop between the concrete bed and lining rings.

## 5 Conclusions

This paper proposes a method for decomposing lining ring displacements in the context of shield tunneling. This decomposition method can process total station monitoring data through separation into three components: dislocation, rotation, and deformation. Because the approach is based on feedback analysis of monitoring data, it is more closely aligned with actual engineering conditions and better facilitates understanding of the components of lining ring displacement. The proposed method was effectively utilized to analyze the displacements of existing tunnels caused by the undercrossing of new tunnels in Phase II of the Shenzhen Metro, Line 11.

Based on certain assumptions, including the functional relationship between the rotation angle and distance, continuity of deformation, and homogeneous circular ring properties, the rotation angle was calculated using deformation–rotation compatibility equations and $z$-direction displacement difference decomposition equations. Then, the dislocation of the lining ring was obtained by removing the rotation effect from the average displacement of the track monitoring points. Subsequently, the deformation of the lining ring was derived by eliminating both the rotation and dislocation components from the measured lining ring displacements. Finally, the calculated values were matched with the coordinates of the monitoring points, and the ellipticity of the lining ring was obtained through curve fitting in MATLAB.

The $z$-direction displacement was revealed as the primary factor affecting the displacement of the lining ring. The $z$-direction displacement of the existing tunnels linearly increases with larger crossing angles, whereas the affected zone decreases nonlinearly. During the undercrossings, the $z$-direction settlement initially rises rapidly and then gradually decreases due to construction measures such as grouting.

Across different crossing angles, the maximum lining ring rotation angle occurs during a 90° undercrossing scenario, and the rotation angles decrease nonlinearly as the crossing angle diminishes. Under a constant crossing angle, the spatiotemporal pattern involves the rotation angle increasing first and then decreasing as the distance from the crossing center increases. Temporally, the rotation angles follow a pattern of initial increase followed by gradual reduction.

Spatially, the lining ring ellipticity increases with crossing angle but decreases with distance from the crossing center. Temporally, two distinct patterns of ellipticity variation were observed. Although both models exhibit similar trends, different crossing angles significantly impact the post-stabilization amplitude fluctuations. Additionally, the long axis of the elliptical

deformation consistently points toward the excavation face of the new tunnel.

In future work, more data will be collected and processed using displacement decomposition methods to derive statistical patterns. This will establish relationships between construction parameters and deformation, which may ultimately help guide construction practices. Moreover, future integration of our computational approach with total station monitoring systems could enable real-time monitoring, calculation, and analysis of tunnel lining displacement. This study provides a robust foundation for real-time early warning systems, offering theoretical support for developing digital twins in tunnel engineering applications. Nonetheless, assumptions behind the proposed model may still introduce errors into the results. Subsequent efforts should therefore also focus on refining these assumptions to enhance the computational accuracy.

## Acknowledgments

This work is supported by the National Natural Science Foundation of China (No. 52090083), the China Railway Southern Technology Development Program, and the Yunnan Provincial Science and Technology Department Science and Technology Program, China (No. 202303AA080003).

## Author contributions

Yiming FU processed the corresponding data and wrote the first draft of the manuscript. Wenqi DING, Zhijian ZHAO, and Wei LONG helped to organize the manuscript. Yafei QIAO revised and edited the final version.

## Conflict of interest

Yiming FU, Wenqi DING, Zhijian ZHAO, Wei LONG, and Yafei QIAO declare that they have no conflict of interest.

## References

Baishya R, Choudhury D, 2025. Dynamic analysis of the effect of vertical clearance on an existing perpendicular crossing tunnel in soil. *Transportation Infrastructure Geotechnology*, 12(4):128. https://doi.org/10.1007/s40515-025-00586-9

Cai YQ, Ying HK, Wang J, et al., 2025. Impact of engineering geological environment on sensor-enabled piezoelectric geocable (SPGC) monitoring performance—accelerated aging test. *Engineering Geology*, 349:107970. https://doi.org/10.1016/j.enggeo.2025.107970

Cao LQ, Fang Q, Zhang DL, et al., 2018. Subway station construction using combined shield and shallow tunnelling method: case study of Gaojiayuan station in Beijing. *Tunnelling and Underground Space Technology*, 82:627-635. https://doi.org/10.1016/j.tust.2018.09.010

Chen RP, Lin XT, Kang X, et al., 2018. Deformation and stress characteristics of existing twin tunnels induced by close-distance EPBS under-crossing. *Tunnelling and Underground Space Technology*, 82:468-481. https://doi.org/10.1016/j.tust.2018.08.059

Dias D, Kastner R, 2013. Movements caused by the excavation of tunnels using face pressurized shields–analysis of monitoring and numerical modeling results. *Engineering Geology*, 152(1):17-25. https://doi.org/10.1016/j.enggeo.2012.10.002

Ding N, Zhou YL, Li DP, et al., 2024. Real-time deformation monitoring of large diameter shield tunnel based on multi-sensor data fusion technique. *Measurement*, 225:114061. https://doi.org/10.1016/j.measurement.2023.114061

Fang Q, Tai QM, Zhang DL, et al., 2016. Ground surface settlements due to construction of closely-spaced twin tunnels with different geometric arrangements. *Tunnelling and Underground Space Technology*, 51:144-151. https://doi.org/10.1016/j.tust.2015.10.031

Fang Q, Zhang DL, Li QQ, et al., 2015. Effects of twin tunnels construction beneath existing shield-driven twin tunnels. *Tunnelling and Underground Space Technology*, 45:128-137. https://doi.org/10.1016/j.tust.2014.10.001

Fang YC, Ni DY, Cai F, et al., 2024. 3D numerical investigation of the interaction between interchange tunnels at different angles. *Heliyon*, 10(5):e27394. https://doi.org/10.1016/j.heliyon.2024.e27394

Galli G, Grimaldi A, Leonardi A, 2004. Three-dimensional modelling of tunnel excavation and lining. *Computers and Geotechnics*, 31(3):171-183. https://doi.org/10.1016/j.compgeo.2004.02.003

Gao BY, Chen RP, Wu HN, et al., 2024. Investigation of mechanical failure performance of a large-diameter shield tunnel segmental ring. *Zhejiang University-SCIENCE A*, 25:411-428. https://doi.org/10.1631/jzus.A2300446

Huang LC, Ma JJ, Lei MF, et al., 2020. Soil-water inrush induced shield tunnel lining damage and its stabilization: a case study. *Tunnelling and Underground Space Technology*, 97:103290. https://doi.org/10.1016/j.tust.2020.103290

Huang MH, Zhou ZL, 2023. Explicit solution analysis of tunnel excavation under existing pipelines on the double-parameter foundation. *Journal of Safety and Environment*, 23(6):1852-1858 (in Chinese). https://doi.org/10.13637/j.issn.1009-6094.2021.2375

Kumar A, Chauhan VB, Kumar P, et al., 2024. Interplay of tunnel geometry and shallow foundation stability in rock: comparative insights into failure modes. *International Journal of Geomechanics*, 24(9):04024185. https://doi.org/10.1061/ijgnai.Gmeng-9815

Lai HP, Zheng HW, Chen R, et al., 2020. Settlement behaviors of existing tunnel caused by obliquely under-crossing shield

tunneling in close proximity with small intersection angle. *Tunnelling and Underground Space Technology*, 97:103258. https://doi.org/10.1016/j.tust.2019.103258

Lee IM, Nam SW, 2001. The study of seepage forces acting on the tunnel lining and tunnel face in shallow tunnels. *Tunnelling and Underground Space Technology*, 16(1): 31-40. https://doi.org/10.1016/s0886-7798(01)00028-1

Li PF, Wang C, Cui XP, et al., 2025. Experimental investigation on the stability of shield tunnel excavation face in upper loose and lower dense water-rich strata. *Zhejiang University-SCIENCE A*, 26:471-491. https://doi.org/10.1631/jzus.A2400309

Li PF, Zhao Y, Zhou XJ, 2016. Displacement characteristics of high-speed railway tunnel construction in loess ground by using multi-step excavation method. *Tunnelling and Underground Space Technology*, 51:41-55. https://doi.org/10.1016/j.tust.2015.10.009

Li XF, Du SJ, Zhang DF, 2012. Analysis on influence of new shield tunneling on closely spaced parallel tunnel. *Chinese Journal of Underground Space and Engineering*, 8(5): 1065-1069 (in Chinese).

Li XG, Chen XS, 2012. Using grouting of shield tunneling to reduce settlements of overlying tunnels: case study in Shenzhen metro construction. *Journal of Construction Engineering and Management*, 138(4):574-584. https://doi.org/10.1061/(asce)co.1943-7862.0000455

Li ZF, Chen ZQ, Yang YJ, et al., 2024. Deformation characteristics of existing tunnels induced by above-crossing quasi-rectangular shield tunnel. *Transportation Geotechnics*, 45:101227. https://doi.org/10.1016/j.trgeo.2024.101227

Lin CG, Zhang ZM, Wu SM, et al., 2013. Key techniques and important issues for slurry shield under-passing embankments: a case study of Hangzhou Qiantang river tunnel. *Tunnelling and Underground Space Technology*, 38:306-325. https://doi.org/10.1016/j.tust.2013.07.004

Liu SH, He MD, Liu JY, 2021. Deformation analysis on the existing shield tunnel obliquely crossed by new tunnel. *Chinese Journal of Underground Space and Engineering*, 17(1):263-272 (in Chinese). https://doi.org/10.20174/j.juse.2021.01.031

Liu X, Fang Q, Zhang DL, et al., 2019. Behavior of existing tunnel due to new tunnel construction below. *Computers and Geotechnics*, 110:71-81. https://doi.org/10.1016/j.compgeo.2019.02.013

Liu X, Zhang R, Fang Q, et al., 2024. Subgrade settlements of existing railway lines and operational parameters of shield machine induced by twin shield tunnel excavations: a case study. *Journal of Central South University*, 31(1):272-287. https://doi.org/10.1007/s11771-023-5447-9

Lo KY, Ramsay JA, 1991. The effect of construction on existing subway tunnels—a case study from Toronto. *Tunnelling and Underground Space Technology*, 6(3):287-297. https://doi.org/10.1016/0886-7798(91)90140-y

Sharifzadeh M, Kolivand F, Ghorbani M, et al., 2013. Design of sequential excavation method for large span urban tunnels in soft ground–Niayesh tunnel. *Tunnelling and Underground Space Technology*, 35:178-188. https://doi.org/10.1016/j.tust.2013.01.002

Shen SL, Wu HN, Cui YJ, et al., 2014. Long-term settlement behavior of metro tunnels in the soft deposits of shanghai. *Tunnelling and Underground Space Technology*, 40: 309-323. https://doi.org/10.1016/j.tust.2013.10.013

Soomro MA, Samo SR, Saand A, et al., 2022. Numerical parametric study of settlement and load transfer mechanism of pile group due to twin stacked tunnelling with different construction sequences. *European Journal of Environmental and Civil Engineering*, 26(3):1064-1096. https://doi.org/10.1080/19648189.2019.1695678

Wanchai T, Cho GC, 2005. Tunnelling in Bangkok–two case studies. *Journal of Korean Tunnelling and Underground Space Association*, 7(2):59-69.

Wei G, Yang B, Wu HJ, et al., 2020. Research on longitudinal deformation of existing shield tunnel caused by shield tunneling. *Chinese Journal of Underground Space and Engineering*, 16(6):1754-1762 (in Chinese).

Wei XJ, Hong WQ, Wei G, et al., 2018. Rotation and shearing dislocation deformation of subway tunnels due to adjacent ground stack load. *Chinese Journal of Rock Mechanics and Engineering*, 37(5):1281-1289 (in Chinese). https://doi.org/10.13722/j.cnki.jrme.2017.1576

Wham BP, Argyrou C, O'Rourke TD, 2016. Jointed pipeline response to tunneling-induced ground deformation. *Canadian Geotechnical Journal*, 53(11):1794-1806. https://doi.org/10.1139/cgj-2016-0054

Wu HN, Shen SL, Liao SM, et al., 2015. Longitudinal structural modelling of shield tunnels considering shearing dislocation between segmental rings. *Tunnelling and Underground Space Technology*, 50:317-323. https://doi.org/10.1016/j.tust.2015.08.001

Yan ZG, Ai SH, Yang X, et al., 2024. Mechanical properties of segmental joints strengthened by assembled reinforcement structures for shield tunnel linings. *Zhejiang University-SCIENCE A*, 25:1037-1050. https://doi.org/10.1631/jzus.A2300455

Yin ML, Jiang H, Jiang YS, et al., 2018. Effect of the excavation clearance of an under-crossing shield tunnel on existing shield tunnels. *Tunnelling and Underground Space Technology*, 78:245-258. https://doi.org/10.1016/j.tust.2018.04.034

Zhang MX, Zhang J, Wu YM, et al., 2019. Analysis of double-line shield tunnel over-crossing subway tunnel in completely weathered rock formation. *China Civil Engineering Journal*, 52(9):100-108 (in Chinese). https://doi.org/10.15951/j.tmgcxb.2019.09.008

Zhang P, Chen RP, Wu HN, et al., 2020. Ground settlement induced by tunneling crossing interface of water-bearing

mixed ground: a lesson from Changsha, China. *Tunnelling and Underground Space Technology*, 96:103224. https://doi.org/10.1016/j.tust.2019.103224

Zhang QF, Xia TD, Ding Z, et al., 2016. Effect of nearby undercrossing tunneling on the deformation of existing metro tunnel and construction control. *Rock and Soil Mechanics*, 37(12):3561-3568 (in Chinese). https://doi.org/10.16285/j.rsm.2016.12.027

Zhang XH, 2020. Study on the Effects of Excavation on the Stress and Deformation of Shield Tunnel Structures. PhD Thesis, Zhejiang University, Hangzhou, China (in Chinese). https://doi.org/10.27461/d.cnki.gzjdx.2020.002738.

Zhang XS, Tan HC, Liu ZH, et al., 2023. Study on the influence of subway tunnel induced by under-crossing tunnel based on monitor data in Shenzhen, China. *Sustainability*, 15(17):13232. https://doi.org/10.3390/su151713232

Zhang ZG, Cheng ZX, Zhang MX, et al., 2022. Dislocation deformation of existing longitudinal tunnel structure induced by shield tunneling by under-crossing considering influence of lining permeability. *China Journal of Highway and Transport*, 35(11):180-194 (in Chinese). https://doi.org/10.19721/j.cnki.1001-7372.2022.11.017

Zhang ZW, Zheng G, Cheng XS, et al., 2024. Analytical approach for longitudinal deformation of shield tunnels considering bending-shear-torsional effects of circumferential joints. *Tunnelling and Underground Space Technology*, 152:105946. https://doi.org/10.1016/j.tust.2024.105946

## Electronic supplementary materials

Tables S1–S4